PHYSICAL REVIEW E **89**, 011001(R) (2014)

Flow-induced structures versus flow instabilities

M. A. Fardin,[1,2,*] C. Perge,[1] N. Taberlet,[1] and S. Manneville[1]

[1]*Université de Lyon, Laboratoire de Physique, École Normale Supérieure de Lyon, CNRS UMR 5672, 46 Allée d'Italie, 69364 Lyon cedex 07, France*

[2]*The Academy of Bradylogists, Paris, France*

(Received 23 September 2013; published 2 January 2014)

The Taylor-Couette flow of a dilute micellar system known to generate shear-induced structures is investigated through simultaneous rheometry and ultrasonic imaging. We show that flow instabilities must be taken into account since both Reynolds and Weissenberg numbers may be large. Before nucleation of shear-induced structures, the flow can be inertially unstable, but once shear-induced structures are nucleated, the kinematics of the flow become chaotic, in a pattern reminiscent of the elastically dominated turbulence known in dilute polymer solutions. We outline a general framework for the interplay between flow instabilities and flow-induced structures.

DOI: 10.1103/PhysRevE.89.011001 PACS number(s): 47.20.−k, 83.80.Qr, 47.27.−i, 47.50.Gj

Fluid dynamics are of interest for many disparate scientists including physicists, chemists, and engineers. Although the goals of these various communities are often congruent, their methods may widely differ. For instance, a strictly "hydrodynamic" approach to fluid dynamics focuses on macroscopic changes in the structure of the flow, i.e., the so-called flow instabilities, often regardless of the fluid which is *de facto* assumed to behave like water ("hydro" in Greek). In contrast, a "rheological" perspective focuses on microscopic changes in the structure of the fluid, i.e., the so-called flow-induced structures, often within viscometric assumptions, i.e., regardless of the possibility for flow instabilities. The ongoing synthesis of the methods of fluid dynamics will inevitably require a framework able to describe both macroscopic changes in the flow field and microscopic changes in the fluid structure. We shall show here that studying flows of micellar surfactant solutions can greatly help to reach that goal.

Beside their tremendous industrial importance in applications such as detergence, oil recovery, and drag reduction, surfactant systems that form rodlike micelles, which can grow to become wormlike and entangled when the concentration increases, have long been used as model systems for rheological research [1–3]. Still, although the dilute regime of rodlike micelles has been extensively studied in the context of highly elastic shear-induced structures (SIS) and associated shear thickening [4–7], here we thoroughly consider the possibility for flow instabilities in such systems. This Rapid Communication fills this gap by showing that two types of instabilities, respectively due to inertia (driven by the classical hydrodynamic Reynolds number Re) and to SIS (driven by the Weissenberg number Wi that quantifies elasticity), are encountered in the flow of a single dilute micellar system. Our goal is to use this example to further strengthen the relevance of a general framework to describe flow instabilities in a complex fluid, as long as flow-induced structural changes of the fluid are properly taken into account in the definitions of both Re and Wi.

The sample under study is made of 0.16 wt. % hexadecyltrimethylammonium p-toluenesulfonate (CTAT) in water. For this system, which has become a benchmark example of dilute micellar fluids [4], shear thickening is found over the range 0.05–0.8 wt. % [6,7]. Figure 1 shows the viscosity η of our sample as a function of the applied shear rate $\dot{\gamma}$ for three different temperatures T, exhibiting the typical behavior of shear-thickening, dilute surfactant systems (see [4] for a review), that is, a zero-shear viscosity close to the viscosity of water; then a jump in η at a characteristic shear rate $\dot{\gamma}_c$ that increases with T; and, finally, a shear-thinning viscosity branch at high shear rates. This behavior was first explained by postulating the formation of SIS [5]: above $\dot{\gamma}_c$, micelles grow in length and undergo a transition from rodlike to wormlike aggregates. This microscopic scenario was later confirmed through neutron-scattering experiments [6]. The shear-induced state can then be shear thinning due to the increasing alignment of the worms. Here, in the absence of direct evidence for microscopic structural changes, we simply infer them from the close similarity between our rheological measurements and a large body of literature [4].

In the present experiments, the fluid is sheared in a Taylor-Couette (TC) device adapted to a rheometer (ARG2, TA Instruments) and with dimensions (height $H = 60$ mm, gap $d = 2$ mm, radius of the inner rotating cylinder $R_i = 23$ mm) that ensure the "small gap approximation," $\Lambda \equiv d/R_i \simeq 0.087 \ll 1$, without any strong end effect at the top and bottom boundaries ($d/H \ll 1$), so that the laminar base flow is a simple shear with $\dot{\gamma} = U/d = \Omega R_i/d$, where U and Ω are the rotor linear and angular velocities, respectively. We recall that in a TC device with inner rotation, Taylor showed that a Newtonian fluid becomes unstable and develops a secondary flow made of toroidal counter-rotating vortices [8]. Larson *et al.* discovered that non-Newtonian fluids can develop a similar vortex flow solely driven by elasticity instead of inertia [9]. In both cases, the instability develops when the Taylor number Ta exceeds a given threshold Ta_c. In the purely inertial case, $\mathrm{Ta} = \Lambda^{1/2}\mathrm{Re}$, with $\mathrm{Re} \equiv \tau_1\dot{\gamma} = (\rho d^2/\eta)(U/d) = \rho d U/\eta$ and $\mathrm{Ta}_c \simeq 41$ [8,10], while in the purely elastic case, $\mathrm{Ta} = \Lambda^{1/2}\mathrm{Wi}$, with $\mathrm{Wi} \equiv \tau_2\dot{\gamma}$, where τ_2 is a characteristic polymeric relaxation time [9,11] instead of the viscous dissipation time τ_1, and $\rho \simeq 10^3$ kg m^{-3} is the fluid density. In the latter case, the value of Ta_c depends on the constitutive relation of the non-Newtonian fluid, e.g., linear stability theory predicts $\mathrm{Ta}_c \simeq 6$ for the upper-convected Maxwell model [9]. More generally, the balance between

*marcantoine.fardin@ens-lyon.fr

 ©2014 American Physical Society

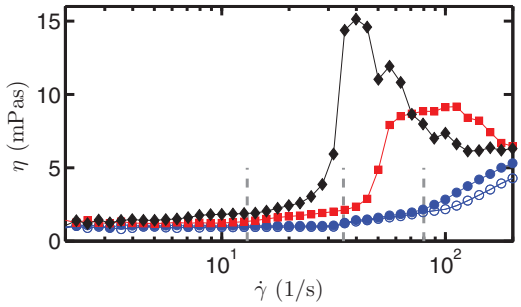

FIG. 1. (Color online) Viscosity η vs shear rate $\dot{\gamma}$ at $T = 20$, 25, and 30 °C (filled symbols, from top left to bottom right) for CTAT at 0.16 wt. % seeded with 1 wt. % polyamide spheres (see text). Open symbols correspond to a CTAT sample free of contrast agents at $T = 30$ °C. The addition of polyamide spheres increases the viscosity by about 15%, but does not change the overall behavior. Data points correspond to averages over the last 5 s of shear rate steps of total duration 15 s. Vertical dashed lines indicate the onset of shear thickening $\dot{\gamma}_c \simeq 13$, 35, and 80 s^{-1}, respectively inferred at $T = 20$, 25, and 30 °C, from start-up experiments of typical duration 500 s.

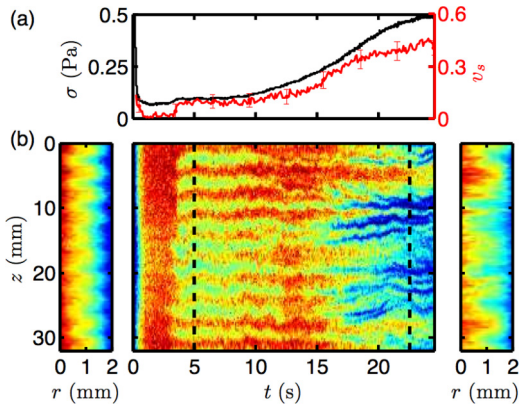

FIG. 2. (Color online) Spatiotemporal dynamics of CTAT at $T = 25$ °C for $\dot{\gamma} = 50$ s^{-1} (see also Movie 1 of Supplemental Material [16]). The flow is first inertially unstable and then elastically unstable due to SIS formation. (a) Global shear stress $\sigma(t)$ measured by the rheometer (in black) and dimensionless slip velocity $v_s(t)$ (in red) [23]. (b) Spatiotemporal diagram (center) of the velocity $v(r_0,z,t)$ at $r_0 = 0.20$ mm from the rotor. The dotted lines show the times $t_0 = 5$ and 22.5 s corresponding to the velocity maps $v(r,z,t_0)$ shown on the left and right, respectively. The color scale is linear and goes from 0 to ΩR_i for the velocity maps and from $0.5\Omega R_i$ to ΩR_i for the diagram. The vertical axis z is oriented downwards with $z = 0$ being taken at about 6 mm from the top of the TC cell.

elasticity and inertia can be estimated by the elasticity number $\mathcal{E} \equiv \mathrm{Wi/Re} = \tau_2/\tau_1$ [12].

Since we expect secondary flows to emerge, our geometry is equipped with a recently developed two-dimensional ultrasonic velocimetry technique that allows the simultaneous measurement of 128 velocity profiles over 30 mm along the vertical direction in the TC geometry [13]. We use ultrafast plane-wave imaging and cross correlation of successive images [14] to infer velocity maps from the echoes backscattered by acoustic contrast agents seeding the fluid, namely 1 wt. % polyamide spheres (Arkema Orgasol 2002 ES 3 Nat 3, mean diameter 30 μm, relative density 1.03), which do not significantly affect the rheological behavior of our solution (see Fig. 1). This technique yields the component $v_y(r,z)$ of the velocity vector, $\mathbf{v} = (v_r, v_\theta, v_z)$ in cylindrical coordinates, projected along the acoustic propagation axis y as a function of the radial distance r to the rotor and of the vertical position z with a temporal resolution down to 50 μs [13]. The acoustic axis y is horizontal and makes an angle $\phi \simeq 10°$ with the normal to the outer cylinder so that $v_y = \cos\phi\, v_r + \sin\phi\, v_\theta$. Finally, we define the measured velocity as $v = \frac{v_y}{\sin\phi} = v_\theta + \frac{v_r}{\tan\phi}$, which coincides with the azimuthal velocity v_θ in the case of a purely azimuthal flow $\mathbf{v} = (0, v_\theta, 0)$. More generally, v combines contributions from both azimuthal and radial velocity components. Nevertheless, close to instability onset, secondary flows are usually much weaker than the main flow, such that $v \simeq v_\theta$ [13,15].

Figure 2 reports the start-up flow of CTAT at $T = 25$ °C for $\dot{\gamma} = 50$ s^{-1} (see also Movie 1 of Supplemental Material [16]). At very short times, a laminar boundary layer extends from the inner cylinder to the outer cylinder. A Taylor vortex flow (TVF) then develops for $t \gtrsim 3$ s, deforming the main flow which becomes periodic along z: slow moving fluid is brought inward in regions of centripetal radial flow and fast moving fluid is pushed outward in regions of centrifugal radial flow. This initial sequence of events would be exactly similar if the fluid was pure water [13,17]. The fact that such a TVF for dilute micelles is reported here should not be surprising since, assuming the fluid to be influenced only by inertia in this initial sequence, we have $\mathrm{Ta} = \Lambda^{1/2}\mathrm{Re} \simeq 60 > \mathrm{Ta}_c$ for $\dot{\gamma} = 50$ s^{-1}. In computing τ_1, we have used the dynamic viscosity relevant to the short-time behavior, i.e., the zero-shear viscosity $\eta_0 \simeq 1$ mPa s. As shown in Fig. 2(a), the onset of TVF at $t \simeq 3$ s corresponds to a slight increase of the shear stress σ (after an initial spike due to the feedback with the rheometer inertia). This first stress increase is simply due to the formation of vortices breaking the viscometric assumption [13]. In contrast, for $t \gtrsim 10$ s, the stress (or, alternatively, the viscosity) climbs up much more dramatically. Since $\dot{\gamma} = 50$ s^{-1} falls into the shear-thickening range for $T = 25$ °C (see Fig. 1) and in view of the literature [4], this next sequence of events can be attributed to slow SIS formation. Meanwhile, the structure of the vortex flow is disrupted. The formerly well-defined wavelength and amplitude of the main flow shown on the left in Fig. 2(b) are lost and the flow becomes chaoticlike on the right in Fig. 2(b). This latter state is reminiscent of the inertioelastic turbulent state called "disordered oscillations" [18] or "elastically dominated turbulence" [19]. While isovelocity lines in the initial state can be approximated by harmonic functions, the secondary flows associated with the SIS deform the main flow intermittently. The state on the right in Fig. 2(b) is representative of the asymptotic turbulent flow. It continuously generates large fluctuations in the viscosity and stress, which have been reported before but are accounted for here in terms of elastic turbulence [4]. Note also that the turbulent nature of the flow can locally and transiently generate plug flow profiles that may explain some earlier one-dimensional (1D) velocity measurements [20,21]. At lower shear rates, e.g., $\dot{\gamma} = 20$ $s^{-1} < \dot{\gamma}_c$ and $\mathrm{Ta} \simeq 24 < 41$, the flow is below both thresholds for TVF and SIS formation and remains purely azimuthal, as shown in the Supplemental Material to Fig. 1 [16].

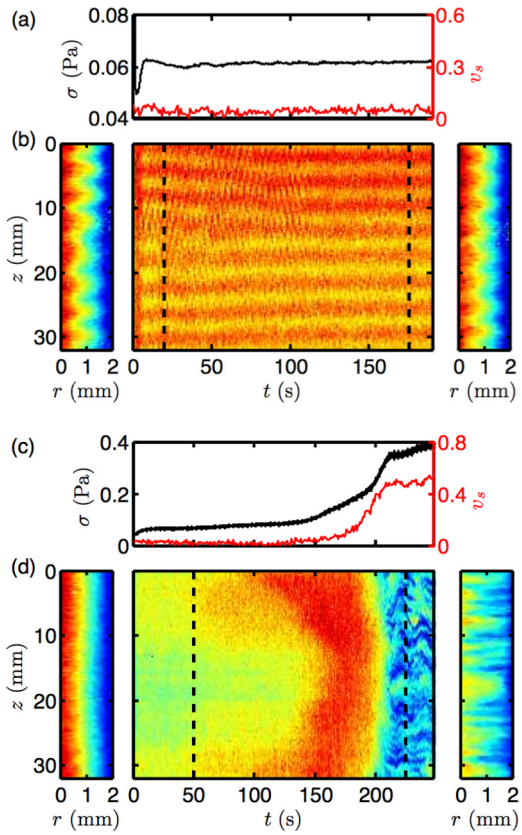

FIG. 3. (Color online) Same as Fig. 2 for (a),(b) $T = 30\,^{\circ}\mathrm{C}$ and $\dot{\gamma} = 40\,\mathrm{s}^{-1}$ showing only inertial instability and (c),(d) $T = 20\,^{\circ}\mathrm{C}$ and $\dot{\gamma} = 20\ \mathrm{s}^{-1}$ where the flow slowly develops SIS and the associated elastically dominated turbulence without initial TVF (see also Movies 2 and 3 of the Supplemental Material, respectively [16]). (b) $r_0 = 0.40$ mm and $t_0 = 20$ (left) and 175 s (right). (d) $r_0 = 0.53$ mm and $t_0 = 50$ (left) and 225 s (right). The color scale goes from 0 to ΩR_i for all velocity maps and from $\Omega R_i/8$ ($\Omega R_i/4$) to ΩR_i for the diagram in (b) [(d)].

As it turned out for $T = 25\,^{\circ}\mathrm{C}$, the critical shear rate $\dot{\gamma}_c$ for SIS formation and the critical shear rate $\dot{\gamma}_{\mathrm{TVF}} \equiv \mathrm{Ta}_c/(\tau_1 \Lambda^{1/2})$ for the onset of TVF are about the same value $\dot{\gamma}_c \simeq \dot{\gamma}_{\mathrm{TVF}} \simeq 35\ \mathrm{s}^{-1}$ in our TC geometry ($\Lambda^{1/2} \simeq 0.29$). In order to separate the inertial TVF and the turbulence associated with SIS more readily, we reproduced similar shear start-up protocols at two other temperatures, $T = 20$ and $30\,^{\circ}\mathrm{C}$, as shown in Fig. 3. Increasing the temperature slightly lowers the zero-shear viscosity (see Fig. 1) so that $\dot{\gamma}_{\mathrm{TVF}}$ only decreases from 45 s^{-1} at $20\,^{\circ}\mathrm{C}$ to 33 s^{-1} at $30\,^{\circ}\mathrm{C}$. In contrast, the same temperature change has a much stronger impact on $\dot{\gamma}_c$. As reported extensively in the literature [4], lowering the temperature leads to easier SIS formation, hence shifting $\dot{\gamma}_c$ to lower values. Figure 1 indicates $\dot{\gamma}_c \simeq 13$ and 80 s^{-1} at $20\,^{\circ}\mathrm{C}$ and $30\,^{\circ}\mathrm{C}$, respectively. Therefore, at the highest temperature, we should be able to observe TVF without SIS, whereas SIS without TVF may be expected at the lowest temperature. This scenario is fully confirmed in Figs. 3(a) and 3(b) and in Figs. 3(c) and 3(d) where spatiotemporal dynamics are compared for shear rates such that $\dot{\gamma}_{\mathrm{TVF}} < \dot{\gamma} < \dot{\gamma}_c$ and $\dot{\gamma}_c < \dot{\gamma} < \dot{\gamma}_{\mathrm{TVF}}$ at $T = 30$ and $20\,^{\circ}\mathrm{C}$, respectively.

The fact that SIS and TVF can occur separately is an indication that these two phenomena are not consequences of one another. SIS do not need TVF to nucleate, which suggests that the out-of-equilibrium growth of the worms is driven by the base shear flow, as usually postulated [4]. Early velocity measurements at a single height z reported that SIS first form at the inner wall and generate significant slip on this wall [20–22]. The dimensionless slip velocities v_s [23] shown in Figs. 2(a) and 3(c) confirm that the onset of wall slip is concomitant with SIS formation, whereas no noticeable wall slip is reported in the presence of TVF alone [see Fig. 3(a)]. Movie 3 of the Supplemental Material [16] also clearly evidences the radial expansion of SIS through the growth of a weakly sheared region from the rotor for $t \simeq 130$–200 s. More distinct is the fact that SIS nucleation is also heterogeneous along $\mathbf{e}_z$. Indeed, Fig. 3(d) shows that SIS nucleate first at the bottom and top edges of the TC device and then progressively fill the gap.

Of course, TVF does not need SIS since it can occur even in simple molecular fluids. Moreover, the spatiotemporal structure of the flow on the right in Figs. 2(b) and 3(d) is very similar so that inertia is dominating the flow instability before SIS formation, while TVF has negligible impact on the asymptotic elastically turbulent flow after SIS nucleation. In a shear-thickening dilute surfactant solution, both τ_1 and τ_2 depend on $\dot{\gamma}$ and t so that Re, Wi, and $\mathcal{E}$ also depend on $\dot{\gamma}$ and t. To illustrate this, we evaluate a bulk-averaged value of $\mathcal{E}$ in the case of Fig. 2 ($T = 25\,^{\circ}\mathrm{C}$ and $\dot{\gamma} = 50\ \mathrm{s}^{-1}$). Assuming the fluid density ρ to remain constant during SIS formation, we first estimate the Reynolds number by $\mathrm{Re} \simeq \dot{\gamma}_t \rho d^2/\eta_t$, where $\dot{\gamma}_t(\dot{\gamma},t) = \dot{\gamma} - v_s(t)\Omega R_i/d$ is the "true" shear rate corrected for wall slip and $\eta_t(\dot{\gamma},t) = \sigma(t)/\dot{\gamma}_t(\dot{\gamma},t)$ the corresponding "true" viscosity. This yields a decrease from $\mathrm{Re} \simeq 200$ before SIS formation to $\mathrm{Re} \simeq 7$ in the final state. Estimating the characteristic viscoelastic time τ_2 of the SIS is more challenging. We take the longest time of the stress relaxation after flow cessation either before or after SIS formation, which yields $\mathrm{Wi} = \dot{\gamma}_t \tau_2 \simeq 0$ before and $\mathrm{Wi} \simeq 100$ after SIS formation, in accordance with the literature [4]. Thus, in the early stages of the dynamics, $\mathcal{E} \simeq 0$, i.e., inertia dominates, whereas after SIS formation, $\mathcal{E} \gtrsim 10$, validating the dominance of elasticity. In some sense, the dynamics of Fig. 2(b) can be seen as the superposition of the dynamics of Figs. 3(b) and 3(d). This superposition appears as rather linear, only because the growth of SIS quickly switches the flow instability from being purely inertia dominated ($\mathcal{E} \ll 1$) to purely elasticity dominated ($\mathcal{E} \gg 1$) [24].

To conclude, the stability diagram of Fig. 4 summarizes the interplay between inertial instability (TVF) and elastic instability of the SIS based on an extensive data set. We believe that such a diagram should be systematically sought in complex fluids subject to flow instabilities in order to sort out the influences of flow-induced microscopic and macroscopic phenomena. Here the purely inertial critical Taylor number Ta_c becomes clearly irrelevant as soon as SIS nucleate. Close to the threshold where both instabilities interact (black lines in Fig. 4), we observe a more complex inertioelastic superposition than the one shown in Fig. 2 further from threshold. A detailed study of this case where $\mathcal{E} \simeq 1$ is left for future work. More generally, the interplay of inertia and elasticity hints to a generalized Taylor number, $\mathrm{Ta} = \Lambda^{1/2} f(\mathrm{Re},\mathrm{Wi})$, with

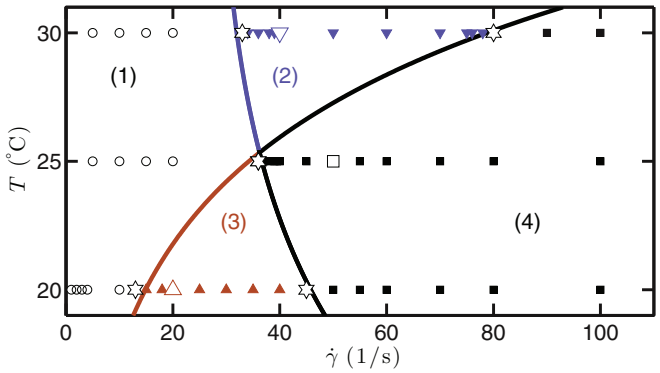

FIG. 4. (Color online) Stability diagram of CTAT. (1) Laminar flow (○). (2) Inertial instability (TVF) without SIS (▼). (3) Elastically dominated instability of the SIS without initial TVF (▲). (4) Elastically dominated instability of the SIS after initial TVF (■). Larger empty symbols correspond to the experiments in Figs. 2 and 3. Stars show the transitions between the various regimes. Solid lines are guides to the eye.

$\lim_{\mathcal{E}\to 0} f(\mathrm{Re},\mathrm{Wi}) = \mathrm{Re}$ and $\lim_{\mathcal{E}\to\infty} f(\mathrm{Re},\mathrm{Wi}) = \mathrm{Wi}$ [25]. Deriving an analytic expression for f and a universal instability criterion accounting for both Re and Wi for any value of $\mathcal{E}$ appears as the next theoretical challenge from which predictions could be drawn for the various boundaries in Fig. 4. The present results show that such an approach should ideally include time dependence in the flow-induced structures. Further experiments on polymer solutions and on more concentrated micellar systems showing shear banding and/or elastic instabilities without SIS formation [26–28] will undoubtedly complete this general physical picture for inertioelastic instabilities and turbulence.

The authors thank S. Lerouge for providing the CTAT sample and for motivating this study. This work was funded by the Institut Universitaire de France and by the European Research Council under the European Union's Seventh Framework Programme No. FP7/2007-2013 and ERC Grant No. 258803.

M.-A.F. and C.P. contributed equally to this work.

[1] H. Rehage and H. Hoffmann, Mol. Phys. **74**, 933 (1991).
[2] J.-F. Berret, in *Molecular Gels* (Springer, Berlin, 2006), pp. 667–720.
[3] M. E. Cates and S. M. Fielding, Adv. Phys. **55**, 799 (2006).
[4] S. Lerouge and J.-F. Berret, Adv. Polym. Sci. **230**, 1 (2010).
[5] H. Rehage and H. Hoffmann, Rheol. Acta **21**, 561 (1982).
[6] R. Gamez-Corrales, J.-F. Berret, L. Walker, and J. Oberdisse, Langmuir **15**, 6755 (1999).
[7] M. Truong and L. Walker, Langmuir **16**, 7991 (2000).
[8] G. Taylor, Phil. Trans. R. Soc. London A **223**, 289 (1923).
[9] R. G. Larson, E. S. G. Shaqfeh, and S. Muller, J. Fluid Mech. **218**, 573 (1990).
[10] R. Donnelly and D. Fultz, Proc. R. Soc. London, Ser. A **258**, 101 (1960).
[11] P. Pakdel and G. H. McKinley, Phys. Rev. Lett. **77**, 2459 (1996).
[12] S. J. Muller, Korea-Aust. Rheol. J. **20**, 117 (2008).
[13] T. Gallot, C. Perge, V. Grenard, M.-A. Fardin, N. Taberlet, and S. Manneville, Rev. Sci. Instrum. **84**, 045107 (2013).
[14] L. Sandrin, S. Manneville, and M. Fink, Appl. Phys. Lett. **78**, 1155 (2001).
[15] M.-A. Fardin, C. Perge, and S. Manneville, arXiv:1307.5415 [cond-mat] [Eur. Phys. J. E (to be published)].
[16] See Supplemental Material at http://link.aps.org/supplmental/10.1103/PhysRevE.89.011001 for a supplementary figure and movies.
[17] A. Akonur and R. M. Lueptow, Phys. Fluids **15**, 947 (2003).
[18] A. Groisman and V. Steinberg, Phys. Rev. Lett. **77**, 1480 (1996).
[19] C. S. Dutcher and S. J. Muller, J. Rheol. **57**, 791 (2013).
[20] S. Koch, T. Schneider, and W. Küter, J. Non-Newt. Fluid Mech. **78**, 47 (1998).
[21] H. Hu, P. Boltenhagen, and D. J. Pine, J. Rheol. **42**, 1185 (1998).
[22] P. Boltenhagen, Y. Hu, E. Matthys, and D. J. Pine, Europhys. Lett. **38**, 389 (1997).
[23] Linear fits of the velocity profiles $v(r,z)$ over about 300 μm in the radial direction r are used to estimate the local shear rates close to each wall and extrapolate the fluid velocities, $v(r=0,z)$ and $v(r=d,z)$. The dimensionless total slip velocity is then defined as $v_s = 1 - [\langle v(0,z)\rangle_z - \langle v(d,z)\rangle_z]/\Omega R_i$ where the average is taken over the 128 simultaneous measurements along the vertical direction z. Error bars in Fig. 2(a) show the standard deviation along z.
[24] The SIS formation time in Fig. 3(d) is much longer than in Fig. 2(b). This is due to the fact that in the first case, $\dot{\gamma} \gtrsim \dot{\gamma}_c$, and it is well known that the formation time of SIS goes according to $(\dot{\gamma} - \dot{\gamma}_c)^{-1}$ [4]. Along the same lines, the apparent wall slip ($\simeq$10%) is visible after the onset of TVF in Fig. 2(a), while it remains negligible in Fig. 3(a). This can be attributed to a larger distance to $\dot{\gamma}_{\mathrm{TVF}}$ in Fig. 2 and to larger effects of radial velocity components on v and v_s.
[25] A. N. Morozov and W. van Saarloos, Phys. Rep. **447**, 112 (2007).
[26] S. M. Fielding, Phys. Rev. Lett. **104**, 198303 (2010).
[27] M.-A. Fardin and S. Lerouge, Eur. Phys. J. E **35**, 1 (2012).
[28] A. Nicolas and A. Morozov, Phys. Rev. Lett. **108**, 088302 (2012).